IEEE Journal of Microwaves

Received 14 September 2020; revised 19 October 2020; accepted 23 October 2020.
Date of current version 7 January 2021.

Digital Object Identifier 10.1109/JMW.2020.3034475

Coherent Automotive Radar Networks: The Next Generation of Radar-Based Imaging and Mapping

MICHAEL GOTTINGER[1] (Member, IEEE), MARCEL HOFFMANN[1] (Graduate Student Member, IEEE), MARK CHRISTMANN[2], MARTIN SCHÜTZ[2], FABIAN KIRSCH[2], PETER GULDEN[2] (Member, IEEE), AND MARTIN VOSSIEK[1] (Fellow, IEEE)

(Invited Paper)

[1]Institute of Microwaves and Photonics (LHFT), Friedrich-Alexander-Universität Erlangen-Nürnberg (FAU), 91058 Erlangen, Germany
[2]Analog Devices Inc., 85579 Neubiberg/Munich, Germany

CORRESPONDING AUTHOR: MICHAEL GOTTINGER (e-mail: michael.gottinger@fau.de).

This work is the result of a cooperation between the Institute of Microwaves and Photonics and Analog Devices Inc. and funded by both partners.

ABSTRACT Imaging radar is a key perception technology for automotive and industrial applications. A lot of progress has been made with high channel count systems, deploying, for example, 12 transmit and 16 receive channels with cascaded monolithic microwave integrated circuit solutions. Nevertheless, fully automated driving requires even higher angular resolution for drive-under/drive-over decisions and exact predictions of object trajectories in dense urban driving scenarios. Both problems can be solved by increasing the antenna size and building larger radars. However, there is a physical limit to what can be placed on the front of a car, and manufacturing very large arrays is quite difficult. Thus, coherent automotive radar networks are a way to achieve high spatial resolution and obtain the complete velocity vector of an object from a single measurement. This solution is commercially attractive, as the sensor can remain relatively small, and complexity can be moved from the physical hardware to algorithms and processing. Two different test setups, each comprised of two multiple-input multiple-output radar units in the 76–77 GHz band, are presented in this article. To obtain azimuth and additional elevation information, the setups use a 1D and a 2D antenna array, respectively. Processing-based coherent evaluation is employed to create an additional radar image with doubled azimuth resolution and improved signal-to-noise ratio and to enable the estimation of vectorial target velocities. These benefits are presented and compared with optical reference images in traffic scenarios.

INDEX TERMS Automotive radar, bistatic radar, FMCW, millimeter wave radar, MIMO radar, multistatic radar, networks.

I. INTRODUCTION

Compared to monostatic radar with a colocated transmitter (TX) and receiver (RX), bistatic or multisite radar systems (MSRSs) provide numerous advantages but with more stringent requirements for cooperative networks [1]. The benefits of such netted arrangements include an increased signal-to-noise ratio (SNR), higher positioning accuracy, velocity vector estimation, improved spatial resolution, and enhanced signal information body. A major drawback is the need for synchronization, frequency and phase, additional data transmission links, higher computational complexity, and accurate station positioning.

Besides lidar, cameras, and ultrasound, automotive radar is one of the key sensing technologies for advanced driver-assistance systems (ADASs) or autonomous driving [2]. State-of-the-art automotive radar sensors are capable of measuring the ranges, radial velocities, azimuth angles, and elevation angles of numerous targets simultaneously and in a fully coherent manner. Furthermore, multiple-input and multiple-output (MIMO) systems are employed to enhance angular estimation

This work is licensed under a Creative Commons Attribution 4.0 License. For more information, see https://creativecommons.org/licenses/by/4.0/

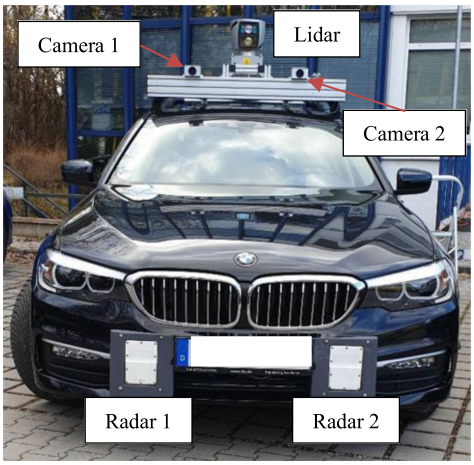

FIGURE 1. Test vehicle with two MIMO radar units, cameras, and a lidar sensor.

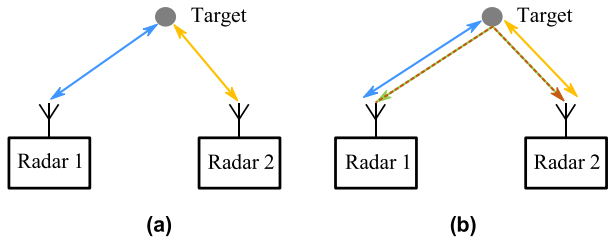

FIGURE 2. Conventional automotive radar setup where each radar is measuring separately (a). Radar network with two cooperating radar units that can measure the cross paths in addition to the two direct paths (b).

TABLE 1. Classification Scheme for Distributed Radar Systems

Class I: Unsynchronized	*Class II:* Synchronized or loosely coupled, incoherent	*Class III:* Synchronized or loosely coupled, coherent features	*Class IV:* Carrier phase and phase noise coherent
Passive bistatic radar [6], [7]	LPR [12], [13]	Carrier phase adjustment [22], [23]	Transponder systems [33]–[37]
RSS based localization [8], [9]	Wireless UWB systems [14], [15]	GPS disciplined oscillators [24], [25]	RF transmission [38], [39]
Multistatic Doppler radar [10], [11]	LPM [16], [17]	DR-FMCW [26]–[28]	Coherent coupling [40]–[42]
	Cooperative FMCW radar networks [18]–[21]	Carrier phase coherence [29], [30]	Wireless sync. link [43], [45]
		Reference target [31], [32]	CFDDS radar [46], [47]

in terms of both accuracy and resolution [3]. Radar sensors with different specifications, e.g., in terms of the maximum detection range, angular resolution, or field of view (FoV), are installed to enable specific safety functionalities. As demonstrated in [4], autonomous test vehicles can be equipped with eight radar sensors and additional stereo cameras for sensing of the environment. Raw data is processed individually to create an object list based on the information from all the sensors.

To apply sophisticated radar networks to the automotive industry, a technology is required that uses all available target information. Precisely, all propagation paths from one This work is licensed under a Creative Commons Attribution 4.0 License. For more information, see https://creativecommons.org/licenses/by/4.0/ transmitting radar to a target and back to another spatially separated receiving radar should be evaluated simultaneously and coherently. Fig. 1 shows a test vehicle for the experimental evaluation of a radar network with two sensors. Furthermore, two cameras and a lidar are used for the sensing of the environment. The direct fusion of radio signals is favorable for detecting and classifying objects in the surrounding area to exhaust the full potential of sensor networks. The principles and advantages of the preferred setup, the orthogonal netted radar system (ONRS), are explained in [5]. The stations of an ONRS operate with distinct waveforms defined by a set of orthogonal codes to ensure perfect separation. A simplified diagram of the key problem is depicted in Fig. 2. The direct paths in (a) can be evaluated with a conventional radar setup. Additionally, the cross paths in (b) should be used for more target information.

To provide an overview of distributed radar concepts in terms of synchronization quality and level of coherence, a classification scheme is introduced in Section II. A brief summary of the coherent full-duplex double-sided (CFDDS) radar concept is given in Section III. Thereafter, Section IV explains a test system setup that allows the operation in practical automotive scenarios. The aperture design and imaging capabilities are shown in Section V. Finally, the test results in Section VI demonstrate the applicability and advantages of coherent automotive radar networks.

II. CLASSIFICATION OF DISTRIBUTED RADAR SYSTEMS

To assess known approaches to spatially distributed radar concepts, we suggest a classification scheme that considers both prerequisites of distributed radar: the degree of synchronization and coherence (Table 1). Distributed radar networks with unsynchronized nodes define *class I*. These systems either measure signals from other sources or create a network of multiple independently working monostatic stations. Passive bistatic radar consists of at least one receiver and a noncooperating transmitter. For example, broadcast and communication signals can be used as "illuminators of opportunity" [6]. To measure bistatic distance and velocity, timing parameters can be determined directly if a line-of-sight (LoS) signal is available. Three-dimensional velocity information can be obtained by using multiple receivers and a fusion of information [7]. Wireless localization results with unsophisticated infrastructure can be obtained by measuring the received signal

strength (RSS) [8]. The comparison of power levels neither involves any timing requirements between wireless nodes nor specific hardware or software [9]. Another example in this class is a multistatic Doppler radar network for the observation of tornadic storms [10] or ionospheric drift velocity [11].

Distributed incoherent radar systems with additional synchronization can be found in *class II*. Providing a temporal reference to one or more nodes of a network can either be accomplished with wireless timing protocols or by physically sharing reference signals. The first option must be chosen for the time of flight (ToF)-based wireless localization to enable much higher precision compared to an RSS estimation. An example of a class II system is the local positioning radar (LPR), which measures the distance between two wireless nodes using frequency modulated continuous wave (FMCW) signals [12]. Up- and down-chirps with increasing bandwidth are exchanged prior to the radar measurement to adjust time and frequency [13]. Wireless localization systems based on comparable synchronization methods but with ultra-wideband (UWB) pulses are explained in [14] and [15]. By employing a reference transponder, the local positioning measurement (LPM) system uses an evaluation of the time difference of arrival (TDOA) and precise 3D positioning becomes feasible [16], [17]. Here, the availability of a reference station eases the synchronization requirements. Based on physical reference signals, loosely coupled radar networks can be employed to obtain additional bistatic range information and improve the detection of passive targets or contour recognition [18]–[21].

Whereas distributed radar in class II provides a stable phase condition only over a small period, i.e., the duration of a single pulse or FMCW chirp, systems in *class III* can use additional coherent features. Coherent radar approaches are favorable to enable a higher integration gain, bistatic or multistatic Doppler measurements and enhanced suppression of stationary clutter, reduction of phase noise (PN) due to the range correlation effect, or interferometry with distributed stations. In contrast to fully coherent radar, systems in this class only allow the use of some of these features. Bistatic radar receivers can perform coherent measurements if the RF carrier is adjusted to the frequency of an illuminator [22]. To this end, stationary clutter can be identified in the Doppler bin that corresponds to the unknown frequency offset of the transmitter and receiver. Phase stabilization methods, which employ motor-controlled phase shifters and auxiliary signal transmission, are discussed in [23]. The RF phase can be stabilized, but mechanical components are much too slow to compensate for oscillator PN. Another way to adjust a stable local oscillator (LO), e.g., based on the rubidium frequency standard, is to employ reference signals broadcasted by the Global Positioning System (GPS) [24]. Here, the pulse per second (PPS) signal provides a time, frequency, and phase reference for a local GPS-disciplined oscillator (GPSDO) and enables coherent integration, e.g., up to one second [25]. All previously mentioned approaches rely on the availability of auxiliary synchronization signals. Based on full duplex transmission, offsets and phase information of the down-converted

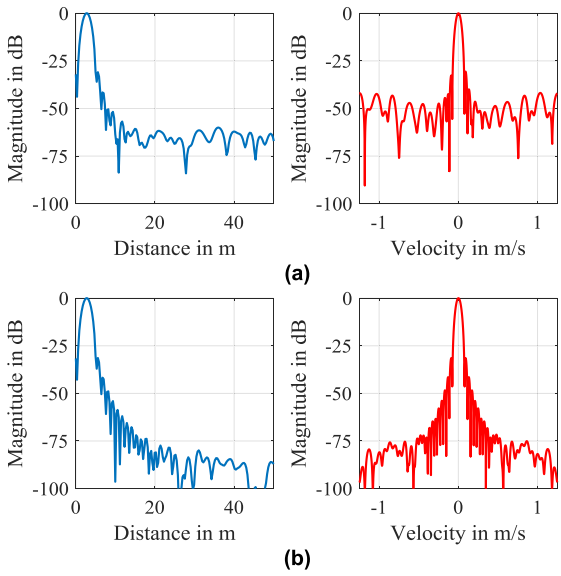

FIGURE 3. **Effect of phase noise (a) in a conventional distributed radar system without phase noise coherency (class I, II and III) and (b) in advanced class IV distributed radar systems with carrier phase and phase noise coherency, as shown in [46].**

intermediate frequency (IF) signals are highly correlated and unknown parameters can be deduced from the analog-to-digital converter (ADC) data [26], [27]. The suppression of correlated PN using the dual-ramp (DR) FMCW enables a ranging standard deviation below 1 cm for distances up to 1 km [28]. Synthetic coherence of the carrier phase can also be established by correction of the unknown initial phases [29], [30]. This method can be used with reference targets or reflection at a dielectric lens [31], [32].

In terms of synchronization quality and coherency, signals of distributed systems in *class IV* are comparable to monostatic radar signals. The influence of uncorrelated PN on a bistatic measurement is shown in Fig. 3(a) in range (blue) and velocity dimension (red). Due to the use of spatially separated signal sources with independent PN, the noise floor in (a) is significantly increased compared to the spectra with phase noise compensation in (b). The level of the remaining noise floor of approx. −80 dB in (b) can compete with monostatic systems. To obtain down-converted signals with a low noise floor, distributed radar systems in class IV require specific hardware components or synchronization steps.

As a first example, systems that use an active backscatter transponder to modulate and retransmit received signals are considered in [33]. Via comparison of two sidebands symmetric to the modulation frequency, coherent wireless localization based on a synthetic aperture approach or suppression of passive clutter [34] becomes possible. This concept has also been applied to detect passive targets with enhanced information [35] and to increase the aperture of a MIMO radar [36]. As an alternative to modulation via RF mixing, switched injection-locked oscillators can also respond coherently [37]. Using the wireless broadcast of reference chirp signals for down-conversion, which is termed over-the-air deramping (OTAD),

accurate synchronization and coherence of multistatic systems can be ensured [38]. A related system concept for distributed detection of passive targets and PN reduction directly transmits the RF carrier for down-conversion at a second station [39]. Phase stable frequency synthesis of quasi-coherent distributed radar is enabled by sharing a reference signal with a frequency close to the desired RF over a wired link in addition to the compensation of the phase difference [40]. Due to low attenuation and available components with high bandwidth, optical links are an option for referencing [40], [41]. Unlike monostatic systems, the PN level is increased by a certain amount if frequency multipliers are employed. Bistatic synthetic aperture radar (SAR) requires long-term phase stability for the generation of a detailed digital elevation model (DEM) [43], [44]. Hence, ultra-stable local oscillators in conjunction with intersatellite links for continuous or pulsed synchronization provide defined phase conditions. Comparable to the class III method in [24], GPS-disciplined crystal oscillators as LOs can be adjusted accurately [45]. Residual phase errors caused by timing jitter are compensated for via post-processing to improve the radar image. The last example for a fully coherent system is the processing-based CFDDS radar method [46]. It allows bistatic or multistatic measurements and derives unknown synchronization parameters from the ADC samples. PN compensation and precise velocity measurements are enabled for localization applications or the detection of passive targets [47].

III. PRINCIPLE OF COHERENT FULL-DUPLEX DOUBLED-SIDED RADAR

Sensor networks based on CFDDS radar offer many advantages compared to the other fully coherent methods in *class IV*. It does not require special components, such as RF cables, optical fibers or converters, or ultra-stable LO clock sources, which are too expensive for automotive applications. Moreover, exchanging synchronization signals or transmitting an additional RF reference over the air in highly dynamic traffic scenarios is very prone to error. Interference from other road users further deteriorates the quality of such approaches. CFDDS radar can derive system offsets, unknown phase values, and the PN profile directly from the ADC samples. Pairwise processing makes this concept flexible enough to use two or more radar units that operate with small timing or frequency offsets to ensure orthogonal multiplexing in the frequency domain. Hence, all prerequisites for an automotive ONRS are fulfilled. As CFDDS radar mainly relies on digital signal processing, it is compatible with state-of-the-art FMCW chirp sequence radar sensors.

A. BRIEF SUMMARY CFDDS-TWR AND SIGNAL MODEL

As we have shown in [46], coherent wireless local positioning is possible with CFDDS two-way ranging (TWR) and coarsely synchronized units. The corresponding signals can be modelled by employing a relative time base, which depends on a timing offset $\Delta\tau$ and an LO drift δ_t. To this end, two radar units simultaneously transmit and receive a sequence of consecutive up- and down-chirps, and samples of the IF signals are transferred to a processing unit. If the sampling criterion is fulfilled, a coherent synthetic beat signal can be created, which is comparable to the monostatic radar signal. By precisely adjusting a voltage-controlled crystal oscillator (VCXO) prior to the radar measurement, computational complexity can be reduced drastically. Instead of up- and down-chirps, a sequence of up-chirps (standard in many automotive radar systems) is enough, and the unambiguous domain along the slow-time dimension is doubled.

Without loss of generality, we explain crucial processing steps and requirements for two radar units, denoted by superscripts. To simplify the equations, a single target is assumed, thermal noise is neglected, and the local oscillators are adjusted to the same frequency, i.e., $\delta_t \approx 0$. Furthermore, the wireless channel is reciprocal and allows identical signal transmission in both directions. The Fourier transform of the IF beat signals can be given as

$$\begin{aligned} S_{k,\mathrm{beat}}^{1/2}(f) = \alpha W\left\{f - \left(\Delta f + \mu\left(\Delta\tau \pm \tau_0\right) \mp f_\mathrm{D}\right)\right\} \\ * \mathcal{F}\left\{\exp\left\{\mathrm{j}\Psi_{\mathrm{pn},k}^{1/2}(t)\right\}\right\} \cdot \exp\left\{\pm \mathrm{j}2\pi f_\mathrm{c}\tau_k\right\} \\ \cdot \exp\left\{\mathrm{j}\left(\varphi_k^1 - \varphi_k^2 + \gamma_k^{1/2}\left(\Delta\tau, \delta_t\right)\right)\right\}, \end{aligned} \tag{1}$$

where α, $W\{\cdot\}$, Δf, f_D, and f_c denote signal magnitude, window function in frequency domain, Doppler frequency, frequency offset, and carrier frequency, respectively [46]. The operators $\mathcal{F}\{\cdot\}$ and $*$ express the Fourier transform in continuous time and convolution, respectively. An FMCW chirp sequence is defined by the chirp number $k \in \{0, \ldots, K-1\}$ and the chirp slope $\mu = B/T_\mathrm{sw}$. RF bandwidth and sweep time are denoted as B and T_sw, respectively. As usual, the ToF τ_k for sufficiently slow targets does not change substantially during the measurement, and the beat frequency in the first line only depends on the initial ToF τ_0. In contrast to monostatic radar, the unknown initial phases $\varphi_k^{1/2}$ do not cancel out, and the influence of the uncorrelated PN $\Psi_{\mathrm{pn},k}^{1/2}(t)$ is much greater. Because of the unknown timing offsets, there is an additional phase shift $\gamma_k^{1/2}(\Delta\tau, \delta_t)$ that depends on the chirp number.

B. APPLICATION TO DISTRIBUTED MIMO SYSTEMS

A setup for a radar network with two MIMO units is depicted in Fig. 4. By choosing a large gap of d_0 between both nodes, a high spatial diversity gain can be achieved, and the accuracy of the lateral velocity estimation is improved. Each radar employs one antenna element for simultaneous transmission and reception (TRX). In this case, the obtained IF spectra can be modelled via (1). Additional TX elements $n \in \{1, \ldots, N\}$ and RX elements $m \in \{1, \ldots, M\}$ are used for the angular estimation. A target is defined by the initial 2D or 3D position $\mathbf{x}_\mathrm{T}$ and the velocity vector $\mathbf{v}_\mathrm{T}$, which is assumed to be constant during a chirp sequence. Different signal paths can be distinguished according to their color. For instance, the direct path (DP) target response $s_{kmn}^{1\to1}(t)$ of the first unit is light blue, and the received cross-path (CP) signal $s_{k11}^{1\to2}(t)$ at unit 2 is red.

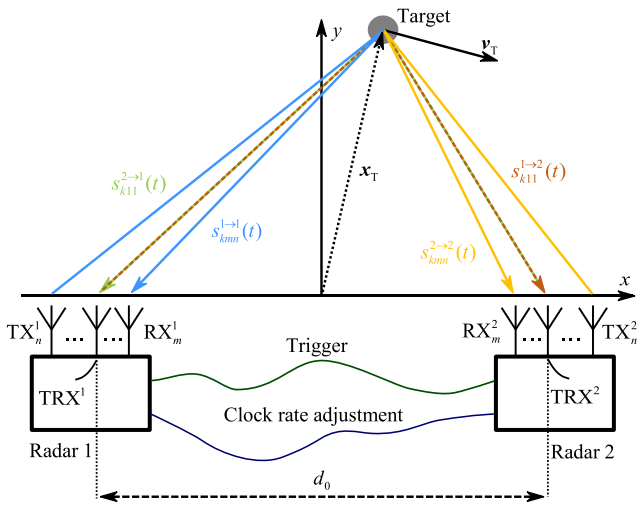

FIGURE 4. Simplified illustration of a network with two radar units physically connected via trigger and system clock. At each unit, one antenna element of the MIMO array is used for simultaneous transmission and reception (TRX-element). Additional transmit (TX) and receive (RX) elements are employed to provide adequate angular resolution.

Physical connections comprise a trigger cable and a MHz signal for adjustment of the LO clock rate. Such a loosely coupled setup ensures precise timing, i.e., the delay $\Delta\tau$ of transmission, reception, and sampling, as well as the frequency offset Δf of radar 2, are clearly defined and stable. Comparable to a wireless system with precisely tuned VCXOs, $\delta_t = 0$ is fulfilled. Regardless of the physical interconnections, the initial phase offsets $\varphi_k^{1/2}$ at the output of a fractional-N phase-locked loop (PLL) are still undefined and need to be corrected [31]. Moreover, synthesizing a GHz RF carrier from the shared MHz reference drastically increases the spectral phase noise density. Frequency multiplication by a factor of u increases the PN density by u^2 [48]. With a high amount of uncorrelated PN impairing the bistatic signals, compensation becomes necessary.

C. REQUIRED PROCESSING STEPS

The beat spectra of both units in (1) are centered around the frequency $f_{\text{shift}} = \Delta f + \mu\Delta\tau$. This shift has to be determined to account for the unknown trigger timing offset, which depends on the internal delay and the trigger cable length. The beat spectra of station 2 are mirrored at f_{shift}, and the complex conjugate is calculated. After removing the offset caused by the frequency shift, targets appear at the same position in both corrected beat signals, and the desired phase information as a function of τ_k is identical. Due to defined timing, the additional phase shift values $\gamma_k^{1/2}(\Delta\tau, \delta_t)$ are constant and can be removed via calibration. Thereafter, the bistatic signals

$$S_{k,\text{beat}}^{1/2}(f) = \alpha W\{f - \mu\tau_0 + f_D\} * \mathcal{F}\left\{\exp\left\{\pm \mathrm{j}\Psi_{\text{pn},k}^{1/2}(t)\right\}\right\} \cdot \exp\{\mathrm{j}(2\pi f_c\tau_k \pm \psi_k)\} \tag{2}$$

are simplified, where ψ_k expresses the unknown initial phase of the FMCW chirps after calibration. To enable coherent measurements, the unknown phases and PN along the fast-time dimension must be compensated for.

Unlike radar localization with single channel sensors and LoS transmission, all targets need to be considered to ensure an adequate SNR. For the bistatic PN, it can be assumed that the influence of $\Psi_{\text{pn},k}^{1/2}(t)$ is comparable, sufficiently small, and independent of the ToF, which can be satisfied using signal sources with high phase stability [49]. Hence, targets can be detected after a fast Fourier transform (FFT), but accuracy is reduced, and the noise floor increases. Assuming L different targets labeled as $\ell \in \{1, \ldots, L\}$, the bistatic signals are given as

$$\begin{aligned}\tilde{S}_{k,\text{beat}}^{1/2}(f) &\approx \exp\{\pm\mathrm{j}\psi_k\} \cdot \mathcal{F}\left\{\exp\left(\pm\mathrm{j}\Psi_{\text{pn},k}(t)\right)\right\} \\ &\quad * \sum_{\ell=1}^{L} \alpha_\ell \exp\left\{\mathrm{j}2\pi f_c\tau_{k,\ell}\right\} \cdot W\left\{f - \mu\tau_{0,\ell} + f_{D,\ell}\right\}\Big) \\ &\approx \exp\{\pm\mathrm{j}\psi_k\} \cdot S_{k,0}(f),\end{aligned} \tag{3}$$

where the target information $S_{k,0}(f)$ is equal in both directions of transmission. To estimate ψ_k, the integral

$$\begin{aligned}\hat{\psi}_k &= -\frac{1}{2}\arg\left\{\int_0^{f_{\max}} \tilde{S}_{k,\text{beat}}^1(f)\left(\tilde{S}_{k,\text{beat}}^2(f)\right)^* df\right\} \\ &= \frac{1}{2}\arg\{\exp\{\mathrm{j}2\psi_k\}\} \cdot \int_0^{f_{\max}} \left|S_{k,0}(f)\right|^2 df = \psi_k + \Phi_k\end{aligned} \tag{4}$$

is evaluated, where the operator $\arg\{\cdot\}$ and the variable $f_{\max}$ denote the angle of a complex value and the upper detectable beat frequency, respectively. The random variable $\Phi_k \in \{0, \pi\}$ accounts for the factor ½ and can be corrected via phase unwrapping along the slow-time dimension [46].

Especially when observing targets with high radar cross-sections (RCSs), phase noise compensation in the fast-time dimension is advantageous. In this case, the remaining PN profile becomes visible and might mask weak targets. Moreover, ranging accuracy is reduced by PN. An estimation in the fast-time dimension

$$\begin{aligned}\hat{\Psi}_{\text{pn},k}(t) &= \frac{1}{2}\arg\left\{\tilde{s}_{k,\text{beat}}^1(t)\left(\tilde{s}_{k,\text{beat}}^2(t)\right)^* \cdot \exp\left\{-\mathrm{j}2\hat{\psi}_k\right\}\right\} \\ &= \frac{1}{2}\arg\left\{\exp\left(\mathrm{j}2\Psi_{\text{pn},k}(t)\right) \cdot \left|\tilde{s}_{k,0}(t)\right|^2\right\}\end{aligned} \tag{5}$$

after correction of the initial phases delivers the phase noise profile for each FMCW chirp. The corresponding time domain beat signals of (3) with the target information $\tilde{s}_{k,0}(t)$ are defined as $\tilde{s}_{k,\text{beat}}^{1/2}(t)$.

As the initial phases and the PN profile are equal for all TX and RX combinations, a correction needs to be applied to all received bistatic signals. Both estimated phase errors in (4) and (5) can therefore be used for compensation via multiplication with the conjugated values to enable fully coherent MIMO operation with separated units.

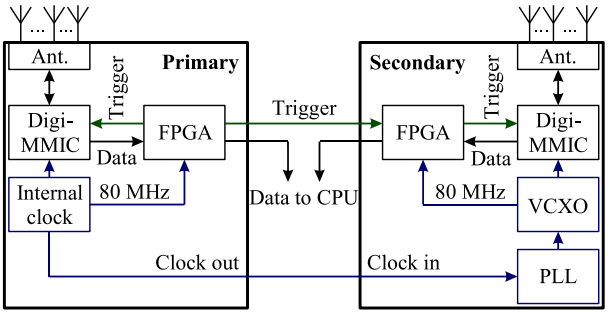

FIGURE 5. Block diagram of the measurement hardware with two MIMO radar units in primary and secondary configuration.

TABLE 2. Key Radar Parameters Used for Measurements

Symbol	Parameter	Value
f_c	RF carrier frequency	76.5 GHz
B	RF bandwidth	1 GHz
T_{sw}	Chirp duration	102.4 µs
μ	Chirp slope	9766 GHz/s
K	Number of FMCW chirps	128
M	Number of RX antennas	4
N	Number of TX antennas	3
f_s	IF Sampling frequency	40 MHz

IV. SYSTEM SETUP

This section provides details on an experimental radar network comprising two FMCW MIMO units. Thereafter, an orthogonal multiplexing scheme and the required calibration steps will be explained.

A. HARDWARE CONFIGURATION

A block diagram of the basic hardware components for a setup with two radar nodes is shown in Fig. 5. The left unit serves as a primary radar node and the right one as a secondary node. In this context, the terms "primary" and "secondary" do not pertain to primary or secondary radar techniques. To enable precise loose coupling and ensure stable timing, the primary node transmits a trigger signal to start a measurement and shares its system clock. To suppress arbitrary interfering signals inside the car, a low PN VCXO is driven by a clock recovery PLL type HMC1013 with a very low loop filter bandwidth. Either the internal or the recovered clock are distributed to all time-sensitive components. To enable coherent fusion of the samples of both units, data is transferred to a central processing unit (CPU). This flexible setup can be extended readily to two or more secondary radar nodes.

The central part is a type ADAR6902 RF system on a chip (SoC) monolithic microwave integrated circuit (MMIC) manufactured by Analog Devices. This fully integrated radar solution is based on the 28 nm complementary metal-oxide-semiconductor (CMOS) process and works in the 76–81 GHz automotive frequency band. To generate FMCW chirps at the desired carrier frequency, an internal 80 MHz crystal oscillator clock f_{clk} and an all-digital PLL (ADPLL) with digital phase detector (DPD), digital loop filter (DLF), and digitally controlled oscillator (DCO) are used to create internal RF signals at approximately 10 GHz. Thereafter, this signal is up converted by a factor of 4 to 40 GHz and can be distributed by an integrated power splitter to cascade multiple ADAR6902 MMICs. A final up-convert stage generates the RF signal in the desired frequency band. Phase noise in the 77 GHz automotive band is specified as −77 dBc/Hz, −100 dBc/Hz, and −120 dBc/Hz for offset frequencies of 100 kHz, 1 MHz, and 10 MHz from the carrier, respectively.

MIMO operation with 3 TX and 4 RX channels is supported. Individual complex in-phase and quadrature (IQ) modulation can be used for the transmit cannels. To this end, a programmable-gain amplifier (PGA) and a 360° phase shifter with variable steps of 2.8° are connected to the TX power amplifier (PA). I and Q components are created by two PGAs. A temperature stabilized maximum TX output power of 14 dBm with up to 63 dB channel gain and a noise figure (NF) lower than 13 dB is usable. Received signals are fed to a low-noise amplifier (LNA) followed by a current-driven mixer for down-conversion. Mixing products with high frequencies and interference are suppressed by a first order low-pass filter (LPF) with 25 MHz cutoff frequency. The internal 16-bit continuous time, oversampling Σ-Δ ADCs support up to 50 mega samples per second (MSPS) per RX channel with 12-bit effective number of bits (ENOB). Continuous time Σ-Δ ADC technology provides excellent inherent alias suppression. To keep optimal system performance, a built-in self-test (BIST) is integrated to perform periodic safety checks.

Patch antennas can be connected via microstrip transmission lines. The required TRX element for CFDDS radar processing is connected to one TX and one RX channel by a Wilkinson power divider. Processing or pre-processing of the raw data can be done internally, or ADC data can be read out. Here, the latter option is preferred to enable beneficial features of coherent radar networks.

All operations are controlled by a Xilinx UltraScale+ field-programmable gate array (FPGA). More specifically, it either provides the trigger signal (primary node) or receives an external trigger (secondary node), starts a measurement, reads out the ADC samples, and is used to transfer data of all nodes to the CPU via Gbit Ethernet.

B. SYSTEM PARAMETERS

The radar properties of the ADAR6902 MMIC can be defined by choosing from a large set of parameters to satisfy the requirements of different automotive applications. For instance, up to 4095 FMCW chirps with 5 GHz RF bandwidth and a chirp slope reaching 1 GHz per 10 µs can be used for a measurement sequence. For our demonstrator setup, parameters according to Table 2 are chosen which allow stable operation. Hence, range resolution, radial velocity resolution, and the unambiguous velocity and are derived as 30 cm, 29.9 cm/s, and ±4.8 m/s, respectively. The influence of loose coupling

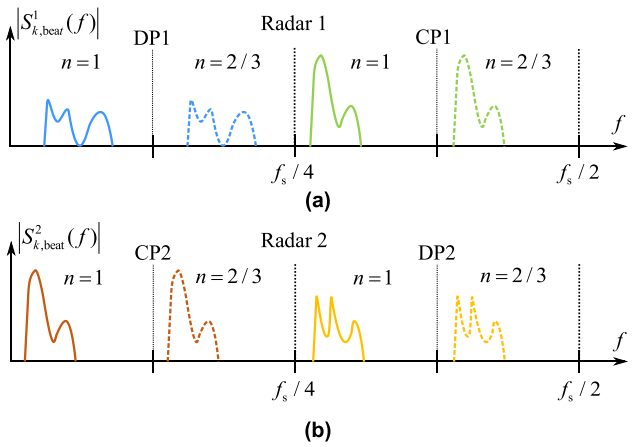

FIGURE 6. Division of the IF beat spectra of radar 1 (a) and radar 2 (b). Down-conversion of signals from TX antenna 1 are depicted as solid lines and as dashed line for TX 2/3. Due to the large spatial separation between both radar units, the observed target responses are different. The RF-mixer of radar 2 uses a frequency offset for improved IF spectral efficiency.

on the bistatic phase noise can be defined in terms of the spectral phase noise density. Deriving the 77 GHz RF carrier from an 80 MHz system clock increases power density of uncorrelated PN by approximately 60 dB.

The used radar driver either allows the recording of raw data for offline evaluation or of at least 10 chirp sequences per second, which are processed with an AMD Ryzen Threadripper CPU and displayed on a laptop for real-time evaluation. Furthermore, sensor data of front and rear cameras, the Velodyne HDL-64 lidar mounted on the roof can be visualized in the rviz tool of the robot operating system (ROS) framework. Additional information on the track is obtained from GPS data and an inertial measurement unit (IMU) in the center console of the test vehicle. Data transmitted over the Controller Area Network (CAN) bus standard. All sensors are synchronized with nanosecond precision by a Precision Time Protocol (PTP) server.

C. MULTIPLEXING OF THE IF SPECTRA

Fig. 6 depicts the IF signals using an orthogonal multiplexing scheme for two radar units, 1 in (a) and 2 in (b), and $N = 3$ TX elements. Colors coincide with individual signal paths in Fig. 4. As phase corrections of the cross-path signals are performed with sampling data of the TRX signal paths $n = 1$ of both radar units (solid lines), the first channel is active during the whole sequence of $K = 128$ FMCW chirps. Time interleaving of the channels $n = 2$ and $n = 3$ (dashed lines), as well as an additional frequency offset of $\Delta f_{\text{FDM}} = \Delta f_{\text{FDM},2/3} = f_s/8$, enables the separation in baseband, where the IF sampling frequency is denoted by f_s. During sweeps with even number k, the first and second TX channels are used simultaneously. The first and third TX channels transmit during sweeps with odd numbers.

The signals received from radar units 1 and 2 are distinguishable because the second radar is operated with a timing offset of $\Delta\tau = f_s/4\mu$. In addition, the primary station is delayed by a small offset that corresponds to the expected trigger offset. To make efficient use of the available IF bandwidth $f_s/2$, a frequency offset of $f_s/4$ is employed for the down-conversion at the RF mixer of the second radar unit. This configuration interchanges cross-path and direct signals in baseband in Fig. 6(b) and lowers the sampling requirements. In summary, the baseband of both radar units is fully occupied, and all different signal components are orthogonal except for out-of-band phase noise in fast-time. Compared to a single chirp sequence radar with one TX, the available unambiguous range is reduced by a factor of 4, and the usable Doppler domain is halved.

D. CALIBRATION

Due to fabrication tolerances of the trigger cable, the exact frequency shift value f_{shift} in Section III.C. is found experimentally and automatically by an initial measurement and a convolution of the beat spectra of units 1 and 2. If the electrical length is influenced by temperature or mechanical stress, adjusted correction values can always be derived from arbitrary measurement data. The antenna arrays are characterized by a complex coupling matrix to model the amplitude and phase imbalances and the cross-coupling of individual elements. To determine the matrix entries, we used the calibration setup and approach described in [50]. For the bistatic measurements, the antenna calibration is factorized in disjoint matrices for TX and RX elements to create cross-calibration matrices. Employing FDM for MIMO multiplexing leads to a phase shift that depends on the TX channel and needs to be corrected to enable accurate beamforming [51]. Time division multiplexing (TDM) based on the interleaving of FMCW chirps at two or more channels causes an additional phase shift as a function of the target velocity, which must be compensated for [52].

V. APERTURE DESIGN, SYNTHESIS AND IMAGING WITH COHERENT RADAR NETWORKS

Assuming far-field conditions, arbitrary MIMO arrays can be described analytically in terms of transmit and receive steering vectors $\mathbf{a}_{\text{TX}}(\beta)$ and $\mathbf{a}_{\text{RX}}(\beta)$, respectively [53]. The variable $\beta = \sin(\theta)$, as a function of the azimuth angle θ, denotes the direction relative to the array. The steering vector of a MIMO radar is therefore given as

$$\mathbf{a}(\beta) = \mathbf{a}_{\text{TX}}(\beta) \otimes \mathbf{a}_{\text{RX}}(\beta), \tag{6}$$

where $\otimes$ denotes the Kronecker product. For a setup with multiple coherently working radar nodes, transmit and receive steering vectors can be extended directly to calculate the steering vector of the whole network. In contrast to FFT-based processing of data sampled by uniform MIMO arrays, more sophisticated methods are required for sparse virtual arrays. Besides conventional beamforming, popular examples are compressed sensing methods [54] and holography (also known as spatial matched filter) [55]. The major drawback of these algorithms is the high computational complexity.

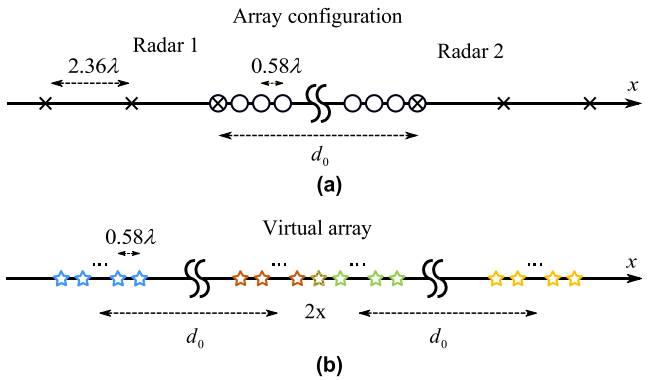

FIGURE 7. Array configuration (a) and corresponding virtual array (b). Both radar units use 3 TX (x) and 4 RX (o) elements. The virtual array (☆) is comprised of three different arrays with a large spatial separation between them. The ULAs with 12 virtual elements on the left and right result from the direct responses. In the center, a ULA with 23 elements is created with the cross-path responses.

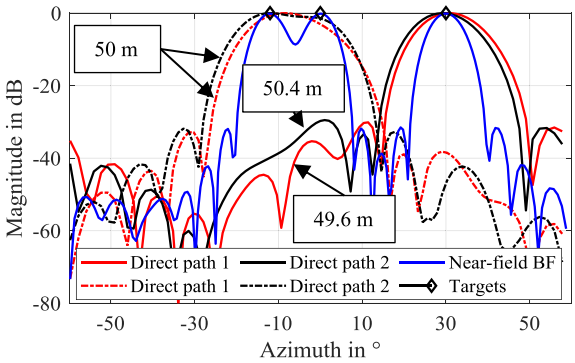

FIGURE 8. The improved resolution capability is assessed with two adjacent and one isolated target (-12°, 0° and 30°). Two cuts of the range-angle map are plotted for the direct paths to account for the geometry. The adjacent targets can only be resolved with the doubled virtual aperture.

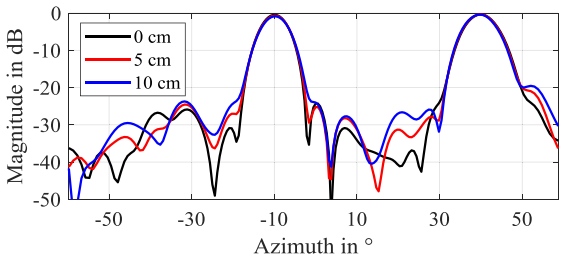

FIGURE 9. Two targets at 4 m from the origin are simulated. Without installation error (black), the SLL is at approximately −24 dB and increases to roughly −21 dB and −20 dB by introducing an error of 5 cm (red) and 10 cm (blue), respectively.

A. STABLE ARRAY CONFIGURATION

The array configuration and the corresponding virtual array of our test system are shown in Fig. 7. The uniform linear arrays (ULAs) with 12 virtual elements on the left and right result from the monostatic responses. In the center, a ULA with 23 elements is created with both cross-path responses. It is equivalent to an additional virtual MIMO radar in the center of the car. Due to the use of two TRX elements, the virtual channel in the center is redundant and can be removed for the angular reconstruction. The spacing between adjacent virtual elements (and RX elements) is set to 0.58λ to create a field of view of ±60°.

Given the radar setup in Fig. 4 and the array configuration in Fig. 7, the resulting virtual array is very sparse due to the large separation $d_0 = 0.86$ m between both radar nodes. Therefore, a reconstruction with all available virtual channels would result in a very fine interference pattern with high sidelobes. To avoid this problem and to minimize computational requirements, the different radar images will be computed individually with all uniform sections of the virtual array. Unlike monostatic systems, the angular reconstruction with both bistatic responses cannot be considered a far-field problem and solved with an FFT. To avoid using iterative methods with high computational effort, we employ delay-and-sum (DAS) beamforming with a Hanning window in conjunction with Tikhonov regularization [56]. This method reduces the sidelobe level and the impact of imperfections such as calibration or antenna array deficiencies. Another difference is that the hypothesis for the reconstruction at equal distance from both bistatic signals depends on the position on an ellipse instead of a circle [57].

B. ANALYSIS VIA SIMULATION

The simulation in Fig. 8 shows the enhanced resolution capability of the doubled virtual array (8.6°) compared to the single MIMO radars (16.4°). To this end, two adjacent targets with an azimuth displacement of 12° and an isolated target, all located at a distance of $d = 50$ m from the origin, are considered. To account for the spatial separation, two different cuts of the direct path range-angle maps are depicted as solid and dashed lines. The isolated target can be detected correctly with all responses, but the resolution ability of the direct path signals is not enough to resolve the two adjacent targets.

A practical problem in automotive applications of distributed radar units may arise due to installation errors caused by, e.g., inaccurate spacing during the manufacturing process or thermal expansion of the bumper or other parts of the car. Fig. 9 shows the reconstruction result with two targets defined by the azimuth angles $\theta_1 = -10°$ and $\theta_2 = 40°$ at $d = 4$ m. Different colors indicate the error-free case (black) and an additional error in d_0 of +5 cm (red) and +10 cm (blue). Nevertheless, both targets can be detected at the correct azimuth angle. The sidelobe level (SLL) increases only slightly from −24 dB to −20 dB. Unlike interferometry, this technique is very robust, as the relative phase difference of bistatic channels is almost unaffected by errors in d_0.

C. VELOCITY VECTOR ESTIMATION AND OVERVIEW

As shown in Fig. 4, two compact radar units are located at the positions $\mathbf{x}_R^{1/2} = (\mp d_0/2, 0)^T$ in a global coordinate system.

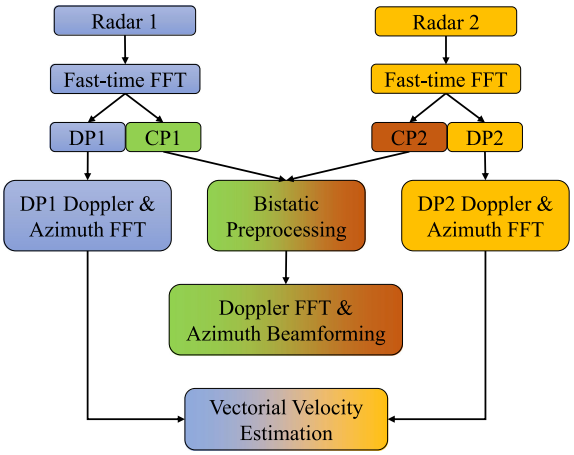

FIGURE 10. Brief overview of coherent signal processing with two radar units. An FFT along the fast-time domain allows the separation of direct-path (DP) and cross-path (CP) signals. The DP signals are processed directly, and the vectorial velocity is determined using both range-angle maps. After preprocessing the CP signals, the slow-time FFT is computed and azimuth beamforming provides doubled resolution.

The measured velocity along corresponding transmission paths $a \rightarrow b$ is modelled by projecting the target velocity on the normalized target vectors as

$$v^{a\rightarrow b} = \langle \mathbf{v}_\mathrm{T}, \mathbf{r}^a \rangle / \|\mathbf{x}_\mathrm{T} - \mathbf{x}_\mathrm{R}^a\| + \langle \mathbf{v}_\mathrm{T}, \mathbf{r}^b \rangle / \|\mathbf{x}_\mathrm{T} - \mathbf{x}_\mathrm{R}^b\|, \quad (7)$$

where $\langle \cdot, \cdot \rangle$, $\mathbf{r}^{a/b}$, and $\| \cdot \|$ denote the standard scalar product, the vector from radar a/b to the target, and the Euclidian distance, respectively [58]. After calculating a range-Doppler map and azimuth beamforming, targets can be identified at the correct position in all radar responses. In contrast to the radial velocity estimation with a single radar unit, the observed velocity differs due to the large spatial separation between the radar units. Hence, the tangential component and the velocity vector can be calculated for each pixel and all targets. Different processing methods for tangential velocity estimation are given in [59].

An overview of the complete signal processing chain for the suggested radar network is depicted in Fig. 10. Colors correspond to the different signal paths in Fig. 4 and IF spectral components in Fig. 6. After division of the IF spectra via fast-time FFT, range-Doppler-azimuth radar images are created directly and separately with the direct path responses of units 1 and 2 by two additional FFTs in Doppler and azimuth. Moreover, transformation from local 2D polar coordinates to a global coordinate system is done to estimate the vectorial velocity of targets. To reconstruct the additional bistatic 3D radar image, signals are shifted in the time-domain to compensate for the exact frequency shift. Now, the phase perturbation of both bistatic mixing products can be determined for all FMCW chirps using the signals of both TRX channels. To cope with phase noise along the fast-time dimension, a sample-wise estimation and compensation is done. After the Doppler FFT, beamforming is used to create a 3D image with doubled angular resolution.

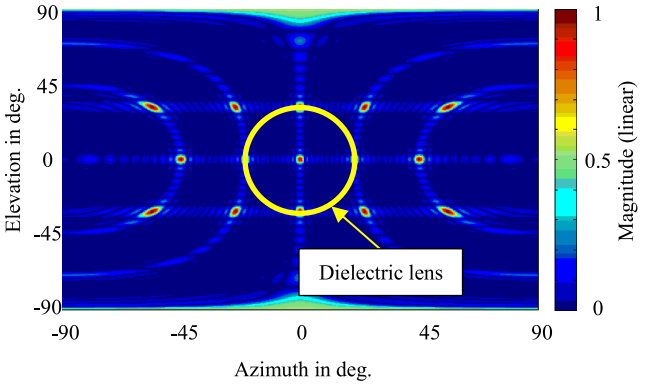

FIGURE 11. Linearly scaled point spread function for the coherent combination of two L-shaped MIMO arrays. The region inside the yellow circle is visible due to the radiation pattern of the lens antennas.

D. 2D ARRAY CONFIGURATION

To resolve targets in azimuth and elevation, we use an L-shaped antenna array with $M = 8$ RXs and $N = 6$ TXs with uniform interelement spacing for both radar units. Here, two cascaded ADAR6902 MMICs are employed in each MIMO radar. Transmit channels are arranged horizontally and receive channels vertically. The virtual array of single MIMO radar is a rectangular uniform array (RLA) with 48 elements. In accordance with the azimuth array in Fig. 7, the array of unit 2 is the mirrored version of the original array. As shown in the 1D case, an additional array with approximately doubled azimuth resolution in the center of the car can be used. For high angular resolution, the interelement spacing is increased to 7.5 mm and 11 mm between the RX and TX elements, respectively. The resulting point spread function (PSF) is depicted in Fig. 11. Here, the resolution of the doubled virtual array in azimuth is increased to 1.7° (no window function in either direction) and 3° are possible in elevation. The resulting grating lobes in Fig. 11 are suppressed by using directive antennas manufactured as dielectric lenses. The unambiguous angular regions are 20° in azimuth and 30° in elevation.

VI. MEASUREMENT RESULTS

To evaluate the aforementioned properties of CFDDS radar, measurements were carried out using two different setups, each consisting of two MIMO FMCW radar stations. The measurement hardware is shown in Fig. 12, where (a) features two *Single DigiMMIC* units with the linear array presented in Fig. 4. The two *Dual DigiMMIC* units in (b) consist of the 2D L-shaped array introduced in Section V.D. Both the trigger and system clock inputs and outputs from Fig. 5 are labelled accordingly. Depending on the particular measurement platform (bumper-mounted on the test vehicle or flexibly mounted on a laboratory cart), the gap d_0 between the stations ranges from 0.5 m to 1.8 m. Radar positioning is always chosen such that the primary unit is on the left side with regard to the radar's viewing direction.

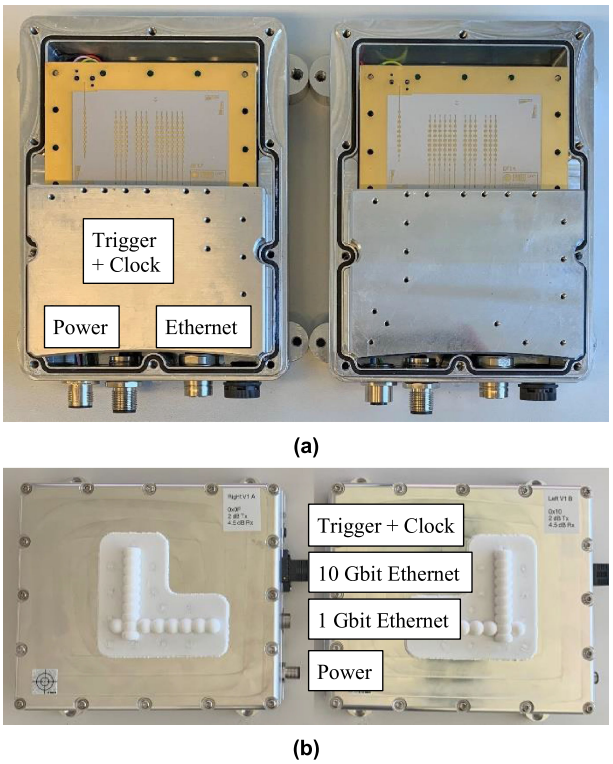

FIGURE 12. **Measurement hardware consisting of two cooperative radar units as a Single DigiMMIC setup with 3 TXs and 4 RXs per unit in (a) and as a Dual DigiMMIC setup with 6 TXs and 8 RXs per unit in (b).**

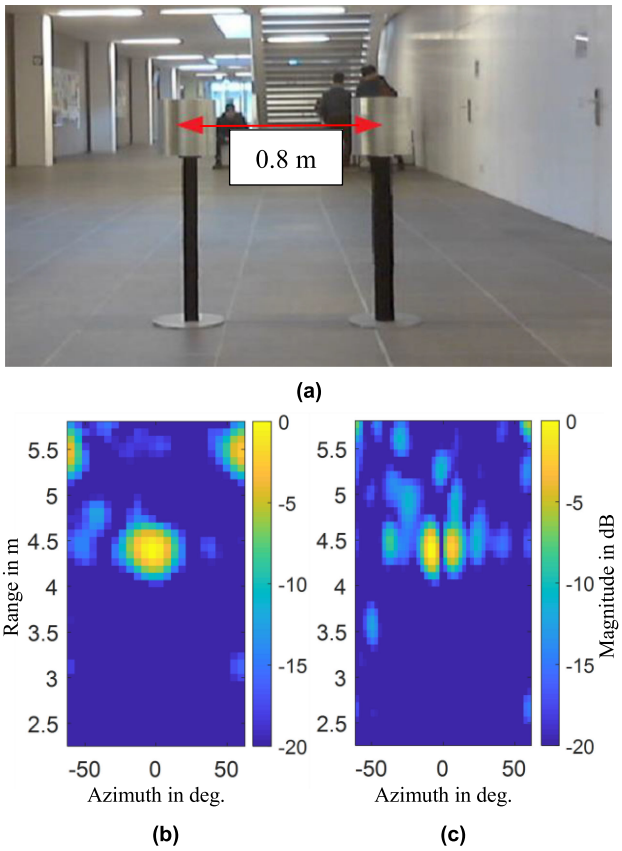

FIGURE 13. **FMCW measurement of a laboratory setup consisting of two metal cylinders spaced at 80 cm (a). The targets cannot be resolved in the conventional monostatic evaluation (b). However, a distinction is possible with the coherent radar network using the CFDDS measuring and evaluation system in (c), thus confirming the enhanced angular resolution.**

To assess the enhanced angular resolution, a Single DigiMMIC measurement with the parameter set from Table 2 was performed in a non-reflective laboratory environment. The gap d_0 between both units was set to 0.97 m. Two metal cylinders, each with a diameter of 24 cm, were positioned 4.23 m from and at an azimuth angle of 0° with respect to the virtual array (see Fig. 13(a)). The cylinder spacing r was set to 0.8 m, which corresponds to an angular difference, $\Delta\theta$, of 10.8°. Under consideration of the deployed Hanning window, $\Delta\theta$ is below the monostatic angular resolution, $\theta_{3\text{dB}}$, of 16.4° for the Single DigiMMIC aperture. This can be observed in the measurement results for a 2D FFT of the conventional beat signals depicted in Fig. 13(b). Consequently, the results of the CFDDS evaluation in (c) confirm the assumption of the improved angular resolution by a factor of 2, as both cylinders can now clearly be resolved.

Theoretically, the doubled number of virtual channels used for the CFDDS radar image improves the SNR by 3 dB compared to a monostatic setup with a single MIMO unit. To assess the performance practically, we conducted measurements with the setup in Fig. 13(a) and replaced the two cylinders with one at 0°. At this azimuth angle, the received and transmitted power is equal along all propagation paths as it is independent from the antenna radiation pattern. The measured SNR of 47 chirp sequences is depicted in Fig. 14 in red (radar network) and blue color (monostatic radar). For each measurement, the noise floor was determined as the average value of

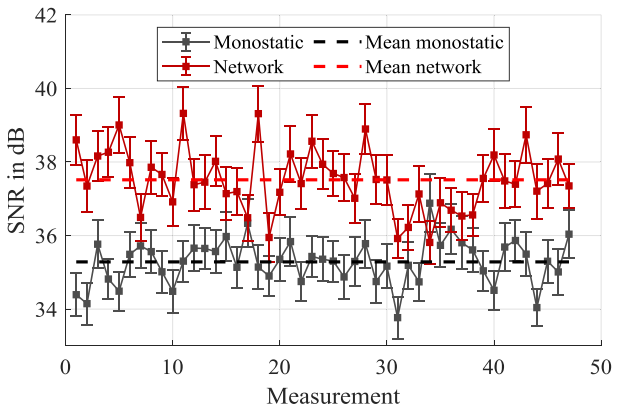

FIGURE 14. **SNR measurements of the radar network (red) compared to a monostatic radar (black). Error bars indicate the standard deviation divided by 10.**

261 empty cells behind the cylinder. Error bars correspond to the measured standard deviation divided by a factor of 10. Dashed lines indicate the mean SNR values of 37.5 dB and 35.2 dB which yields an improvement of 2.3 dB. This result is comparable to the theoretical value. The deviation might be caused by hardware imperfections or multipath propagation.

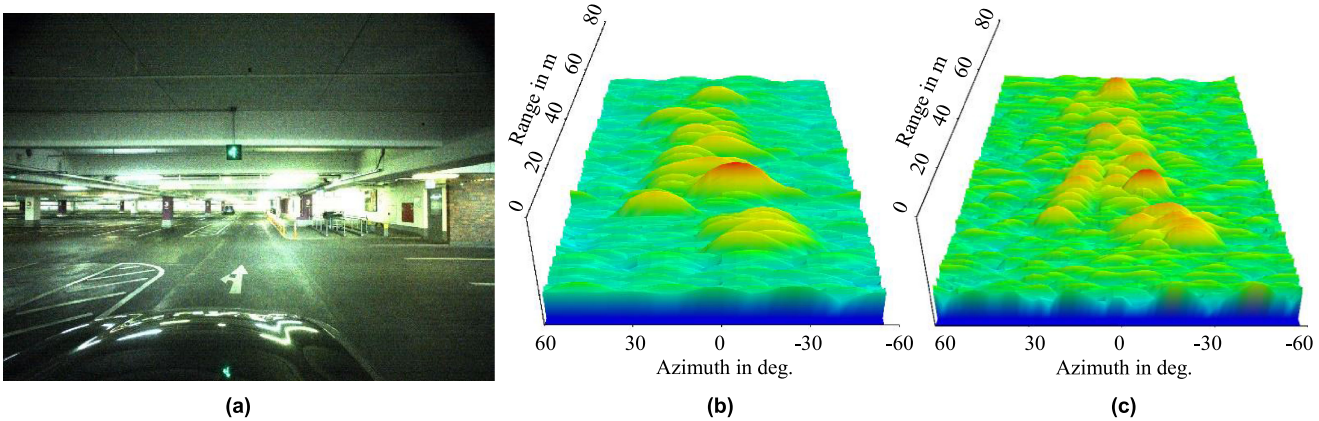

FIGURE 15. FMCW measurement inside the parking garage (a). The column of posts and the shopping carts in the monostatic evaluation (b) are displayed with an inferior resolution and with fewer reflection points than the corresponding CFDDS result (c). Colors red and blue of the normalized logarithmic scale correspond to values of 0 dB and −90 dB, respectively.

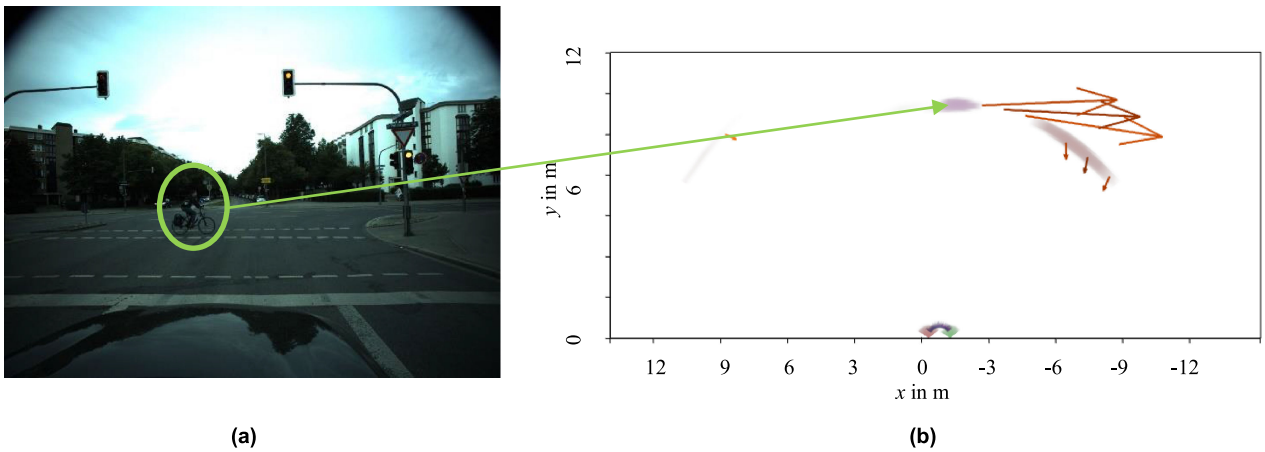

FIGURE 16. Determination of the vectorial velocity of a cyclist traversing an intersection in a single measurement (a). The vectorial velocities of all detected targets are displayed by arrows, whereby the arrow length corresponds to the target's speed (b).

The enhanced azimuth resolution combined with the increased SNR shows great benefit in dynamic, multi-target automotive scenarios. For this, tests were conducted with test vehicle depicted in Fig. 15 and the parameters and hardware setup described in Section IV.B. It features two Single DigiMMIC radar units mounted at the height of the license plate (approximately 0.4 m) and a gap, d_0, of 0.86 m. The measurements were conducted in the highly reflective parking garage shown in Fig. 15(a), which represents a very challenging environment with smooth walls and mirroring targets. To emphasize the improvement produced by the proposed approach, the range-angle representation of the conventional monostatic radar is shown in Fig. 15(b) and contrasted with the CFDDS result in Fig. 15(c). One easily perceptible key feature is the enhanced resolution, especially around the posts on the right-hand side. Furthermore, the overall number of targets is increased as there are additional reflection points that can be detected over the cross path between both stations due to the increased resolution. Based on these two effects, gridmapping and, by extension, contour detection, object classification and tracking, ego-motion estimation, and simultaneous localization and mapping (SLAM) algorithms could be greatly improved.

The instantaneous estimation of both a target's tangential velocity and, consequently, its complete velocity vector is another major advantage of CFDDS-radar imaging and was also evaluated using the test vehicle. The measurements indicate that this feature is advantageous in all dynamic traffic situations. Fig. 16(a) shows a paradigmatic example of a cyclist traversing an intersection. To obtain the vectorial velocity, the associated FMCW measurement is first conventionally processed. Then, customized CFAR-detection is applied to the resulting range-Doppler-azimuth space. Finally, the velocity vectors for the detected targets are determined according to Section V.C. The overlay plot in Fig. 16(b) depicts the velocity vectors from the perspective of the test vehicle. In this figure, the traversing object is prominent. Driver assistance systems could readily use this information to validate or improve

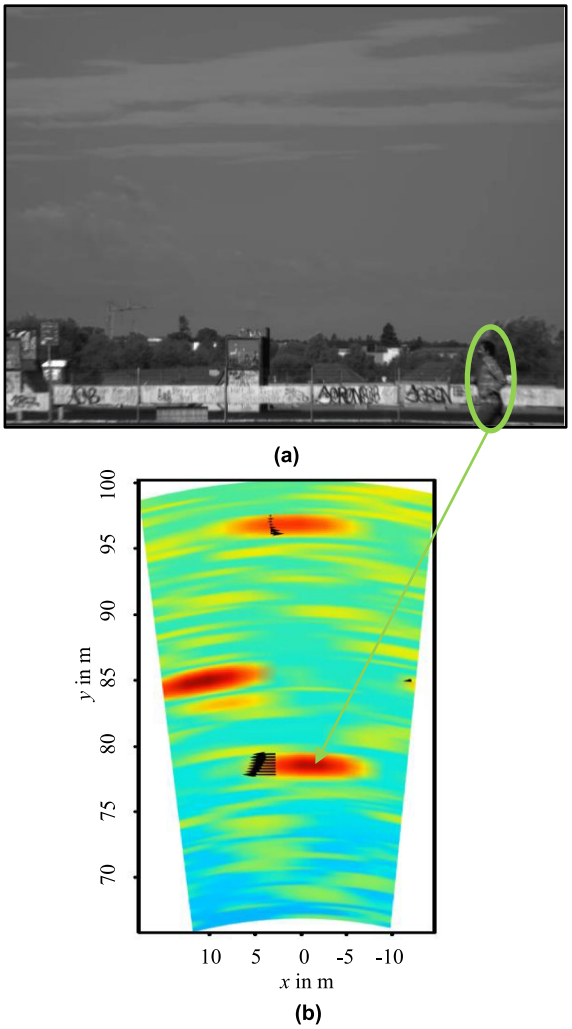

FIGURE 17. **Determination of the vectorial velocity of a transversely jogging pedestrian in a distance of 78 m (a). Again, the arrow length of the velocity vectors in (b) corresponds to the target's speed.**

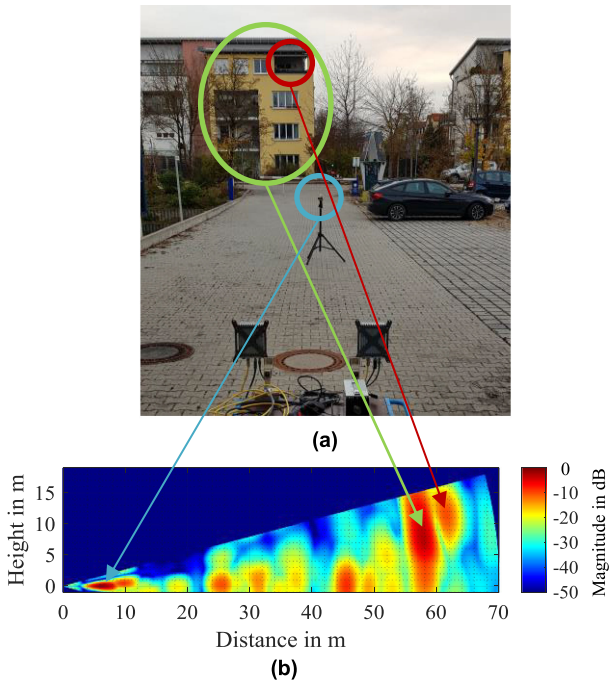

FIGURE 18. **Elevation measurement setup with the Dual DigiMMIC network (a) and normalized radar image with height information (b). Reflections of a corner reflector (blue), a building (green) and a balcony (red) are marked.**

predictions and to increase the safety of both occupants and vulnerable road users. Also, AI-based object classification and tracking can profit from the instantaneous knowledge of the complete velocity vectors.

With the Dual DigiMMIC setup from Fig. 12(b) it is also possible to determine the velocity vector of a target in large distances up to approximately 250 m. Fig. 17(a) depicts a demonstration that was performed on an airfield with a pedestrian jogging transversely to the radar's line of sight in a distance of 78 m. The corresponding overlay plot in Fig. 17(b) shows the velocity vectors of the detected targets. In combination with the improved angular resolution, long-range radar applications including adaptive cruise control (ACC) can greatly be improved using precise vectorial velocity information on the one hand. On the other hand, a very high angular resolution is inevitable to achieve the required lateral resolutions in distances surpassing 50 m or 100 m. Driver assistance systems in general could readily use the enhanced target information to validate or improve predictions and to increase the safety of both occupants and vulnerable road users. In addition, AI-based object classification and tracking can profit from the instantaneous knowledge of the complete velocity vectors.

The height estimation of objects delivers crucial information for advanced driving assistance functions. Automated decisions in practical situations, such as driving through a tunnel or bridge, cannot be made based on 1D angle measurements. To demonstrate this feature, two Dual DigiMMIC radar units are installed 1m above the ground, see Fig. 18(a). A corner reflector in a distance of 7m at the same height serves as reference target. Fig. 18(b) shows the radar image of targets above ground. Besides the corner reflector, a building at 58 m can be observed as distributed target with its maximum at a height of 8.5 m. A second reflection is visible approx. 4 m behind the first one at a height of 11.5 m above the ground. It is caused by the balcony which is comparable to a large dihedral reflector.

VII. CONCLUSION

We have shown that an orthogonal netted radar system for advanced automotive safety functions can be built based on integrated state-of-the-art FMCW MIMO radar sensors. By correctly defining offsets, all different signal paths can be used and evaluated coherently. Our radar demonstrator allows centralized real-time computation and fusion with data from other time-synchronized sensors. Besides the presented setup

with two radar units and an additional doubled aperture, future autonomous cars with numerous radar modules can benefit from this method to obtain additional information. Especially high angular resolution for long-range applications can be achieved by employing more than two modules that operate coherently.

REFERENCES

[1] V. S. Chernyak, *Fundamentals of Multisite Radar Systems: Multistatic Radars and Multiradar Systems*. New York, NY, USA: Gordon & Breach, 1998.

[2] S. Patole, M. Torlak, D. Wang, and M. Ali, "Automotive radars: A review of signal processing techniques," *IEEE Signal Process. Mag.*, vol. 34, no. 2, pp. 22–35, Mar. 2017.

[3] F. Roos, J. Bechter, C. Knill, B. Schweizer, and C. Waldschmidt, "Radar sensors for autonomous driving," *IEEE Microw. Mag.*, vol. 20, no. 9, pp. 58–72, Sep. 2019.

[4] J. Ziegler *et al.*, "Making bertha drive—An autonomous journey on historic route," *IEEE Intell. Transp. Syst. Mag.*, vol. 6, no. 2, pp. 8–20, Summer 2014.

[5] H. Deng, "Orthogonal netted radar systems," *IEEE Aerosp. Electron. Syst. Mag.*, vol. 27, no. 5, pp. 28–35, May 2012.

[6] H. D. Griffiths, "From a different perspective: Principles, practice and potential of bistatic radar," in *Proc. Int. Conf. Radar*, 2003, pp. 1–7.

[7] S. Satoh and J. Wurman, "Accuracy of wind fields observed by a bistatic Doppler radar network," *J. Atmos. Ocean. Technol.*, vol. 20, no. 8, pp. 1077–1091, 2003.

[8] N. Patwari, R. J. O'Dea, and Y. Wang, "Relative location in wireless networks," in *Proc. IEEE VTS 53rd Veh. Technol. Conf.*, 2001, pp. 1149–1153.

[9] A. J. Weiss, "On the accuracy of a cellular location system based on RSS measurements," *IEEE Trans. Veh. Technol.*, vol. 52, no. 6, pp. 1508–1518, Nov. 2003.

[10] P. S. Ray, C. L. Ziegler, W. Bumgarner, and R. J. Serafin, "Single- and multiple-Doppler radar observations of tornadic storms," *Amer. Meteorol. Soc.*, vol. 108, no. 10, pp. 1607–1625, 1980.

[11] G. N. Taylor, H. Rishbeth, and P. J. S. Williams, "Multistatic incoherent scatter measurements of ionospheric drift velocity," *Nature*, vol. 242, pp. 109–111, 1973.

[12] S. Roehr, P. Gulden, and M. Vossiek, "Precise distance and velocity measurement for real time locating in multipath environments using a frequency-modulated continuous-wave secondary radar approach," *IEEE Trans. Microw. Theory Techn.*, vol. 56, no. 10, pp. 2329–2339, Oct. 2008.

[13] S. Roehr, P. Gulden, and M. Vossiek, "Method for high precision clock synchronization in wireless systems with application to radio navigation," in *Proc. IEEE Radio Wireless Symp.*, 2007, pp. 1–4.

[14] C. Zhang, M. J. Kuhn, B. C. Merkl, A. E. Fathy, and M. R. Mahfouz, "Real-time noncoherent UWB positioning radar with millimeter range accuracy: Theory and experiment," *IEEE Trans. Microw. Theory Techn.*, vol. 58, no. 1, pp. 9–20, Jan. 2010.

[15] S. Kong, S. Lee, C. Y. Kim, and S. Hong, "Wireless cooperative synchronization of coherent UWB MIMO radar," *IEEE Trans. Microw. Theory Techn.*, vol. 62, no. 1, pp. 154–165, Jan. 2014.

[16] A. Stelzer, K. Pourvoyeur, and A. Fischer, "Concept and application of LPM—A novel 3-D local position measurement system," *IEEE Trans. Microw. Theory Techn.*, vol. 52, no. 12, pp. 2664–2669, Dec. 2004.

[17] R. Pfeil, S. Schuster, and A. Stelzer, "Optimized parameter estimation for the LPM local positioning system," *IEEE Trans. Instrum. Meas.*, vol. 62, no. 1, pp. 153–166, Jan. 2013.

[18] A. Frischen, J. Hasch, and C. Waldschmidt, "Performance degradation in cooperative radar sensor systems due to uncorrelated phase noise," in *Proc. 11th Eur. Radar Conf.*, 2014, pp. 241–244.

[19] A. Frischen, J. Hasch, and C. Waldschmidt, "Contour recognition with a cooperative distributed radar sensor network," in *Proc. IEEE MTT-S Int. Conf. Microw. Intell. Mobility*, 2015, pp. 3–6.

[20] A. Frischen, J. Hasch, D. Jetty, M. Girma, M. Gonser, and C. Waldschmidt, "A low-phase-noise 122-GHz FMCW radar sensor for distributed networks," in *Proc. 13th Eur. Radar Conf.*, 2016, pp. 49–52.

[21] A. Frischen, J. Hasch, and C. Waldschmidt, "A cooperative MIMO radar network using highly integrated FMCW radar sensors," *IEEE Trans. Microw. Theory Techn.*, vol. 65, no. 4, pp. 1355–1366, Apr. 2017.

[22] E. C. Thompson, "Bistatic radar noncooperative illumination synchronization techniques," in *Proc. IEEE Nat. Radar Conf.*, 1989, pp. 29–34.

[23] M. C. Thompson, L. E. Wood, D. Smith, and W. B. Grant, "Phase stabilization of widely separated oscillators," *IEEE Trans. Antennas Propag.*, vol. 16, no. 6, pp. 683–688, Nov. 1968.

[24] D. E. Fossler, "GPS synchronized disciplined rubidium frequency standard," in *Proc. 21th Annu. Precise Time Time Interval Syst. Appl. Meet. (PTTI)*, 1989, pp. 145–148.

[25] J. S. Sandenbergh and M. R. Inggs, "Synchronizing network radar using all-in-view GPS-disciplined oscillators," in *Proc. IEEE Radar Conf.*, 2017, pp. 1640–1645.

[26] S. Scheiblhofer, S. Schuster, M. Jahn, R. Feger, and A. Stelzer, "Performance analysis of cooperative FMCW radar distance measurement systems," in *IEEE MTT-S Int. Microw. Symp. Dig.*, 2008, pp. 121–124.

[27] R. Feger, C. Pfeffer, W. Scheiblhofer, C. M. Schmid, M. J. Lang, and A. Stelzer, "A 77-GHz cooperative secondary radar system for local positioning applications," in *IEEE/MTT-S Int. Microw. Symp. Dig.*, 2012, pp. 1–3.

[28] W. Scheiblhofer, S. Scheiblhofer, J. O. Schrattenecker, S. Vogl, and A. Stelzer, "A high-precision long range cooperative radar system for rail crane distance measurement," in *Proc. 11th Eur. Radar Conf.*, 2014, pp. 305–308.

[29] R. Feger, C. Pfeffer, W. Scheiblhofer, C. M. Schmid, M. J. Lang, and A. Stelzer, "A 77-GHz cooperative radar system based on multi-channel FMCW stations for local positioning applications," *IEEE Trans. Microw. Theory Techn.*, vol. 61, no. 1, pp. 676–684, Jan. 2013.

[30] R. Feger, C. Pfeffer, C. M. Schmid, M. J. Lang, Z. Tong, and A. Stelzer, "A 77-GHz FMCW MIMO radar based on loosely coupled stations," in *Proc. 7th German Microw. Conf.*, 2012, pp. 1–4.

[31] A. Dürr, R. Kramer, D. Schwarz, M. Geiger, and C. Waldschmidt, "Calibration-based phase coherence of incoherent and quasi-coherent 160-GHz MIMO radars," *IEEE Trans. Microw. Theory Techn.*, vol. 68, no. 7, pp. 2768–2778, Jul. 2020.

[32] S. Edstaller and D. Mueller, "Vector velocity and position measurement using a 77-GHz cooperative radar system," in *Proc. IEEE MTT-S Int. Microw. Symp.*, 2019, pp. 548–551.

[33] M. Vossiek, A. Urban, S. Max, and P. Gulden, "Inverse synthetic aperture secondary radar concept for precise wireless positioning," *IEEE Trans. Microw. Theory Techn.*, vol. 55, no. 11, pp. 2447–2453, Nov. 2007.

[34] S. Müller and A. R. Diewald, "Cooperative radar with signature method for unambiguity," *Adv. Radio Sci.*, vol. 17, pp. 27–34, 2019.

[35] B. Meinecke, M. Steiner, J. Schlichenmaier, and C. Waldschmidt, "Instantaneous target velocity estimation using a network of a radar and repeater elements," in *Proc. 16th Eur. Radar Conf.*, 2019, pp. 241–244.

[36] B. Meinecke, M. Steiner, J. Schlichenmaier, J. Hasch, and C. Waldschmidt, "Coherent multistatic MIMO radar networks based on repeater tags," *IEEE Trans. Microw. Theory Techn.*, vol. 67, no. 9, pp. 3908–3916, Sep. 2019.

[37] M. Vossiek and P. Gulden, "The switched injection-locked oscillator: A novel versatile concept for wireless transponder and localization systems," *IEEE Trans. Microw. Theory Techn.*, vol. 56, no. 4, pp. 859–866, Apr. 2008.

[38] M. Ash, M. Ritchie, K. Chetty, and P. V. Brennan, "A new multistatic FMCW radar architecture by over-the-air deramping," *IEEE Sensors J.*, vol. 15, no. 12, pp. 7045–7053, Dec. 2015.

[39] A. Dürr, B. Schweizer, J. Bechter, and C. Waldschmidt, "Phase noise mitigation for multistatic FMCW radar sensor networks using carrier transmission," *IEEE Microw. Wireless Compon. Lett.*, vol. 28, no. 12, pp. 1143–1145, Dec. 2018.

[40] M. Zhan, X. Xie, H. Yao, R. Xu, and W. Lin, "A novel full phase-coherent frequency synthesis method for SFWF radar application," *IEEE Trans. Microw. Theory Techn.*, vol. 59, no. 7, pp. 1840–1845, Jul. 2011.

[41] S. Futatsumori, K. Morioka, A. Kohmura, K. Okada, and N. Yonemoto, "Design and field feasibility evaluation of distributed-type 96 GHz FMCW millimeter-wave radar based on radio-over-fiber and optical frequency multiplier," *J. Lightw. Technol.*, vol. 34, no. 20, pp. 4835–4843, Oct. 2016.

[42] D. H. Shin, D. H. Jung, D. C. Kim, J. W. Ham, and S. O. Park, "A distributed FMCW radar system based on fiber-optic links for small drone detection," *IEEE Trans. Instrum. Meas.*, vol. 66, no. 2, pp. 340–347, Feb. 2017.
[43] G. Krieger *et al.*, "TanDEM-X: A satellite formation for high-resolution SAR interferometry," *IEEE Trans. Geosci. Remote Sens.*, vol. 45, no. 11, pp. 3317–3341, Nov. 2007.
[44] M. Younis, R. Metzig, and G. Krieger, "Performance prediction of a phase synchronization link for bistatic SAR," *IEEE Geosci. Remote Sens. Lett.*, vol. 3, no. 3, pp. 429–433, Jul. 2006.
[45] W. Q. Wang, "GPS-based time & phase synchronization processing for distributed SAR," *IEEE Trans. Aerosp. Electron. Syst.*, vol. 45, no. 3, pp. 1040–1051, Jul. 2009.
[46] M. Gottinger, F. Kirsch, P. Gulden, and M. Vossiek, "Coherent full-duplex double-sided two-way ranging and velocity measurement between separate incoherent radio units," *IEEE Trans. Microw. Theory Techn.*, vol. 67, no. 5, pp. 2045–2061, May 2019.
[47] A. Frischen, G. Hakobyan, and C. Waldschmidt, "Coherent measurements with MIMO radar networks of incoherent FMCW sensor nodes," *IEEE Microw. Wireless Compon. Lett.*, vol. 30, no. 7, pp. 721–724, Jul. 2020.
[48] M. Abdo, "A low-phase noise frequency multiplier chain," *J. EAEA*, vol. 8, no. 5, pp. 23–33, 1989.
[49] M. C. Budge and M. P. Burt, "Range correlation effects in radars," in *Proc. Rec. IEEE Nat. Radar Conf.*, 1993, pp. 212–216.
[50] C. Schmid and C. Pfeffer, "An FMCW MIMO radar calibration and mutual coupling compensation approach," in *Proc. 10th Eur. Radar Conf.*, 2013, pp. 13–16.
[51] M. Steinhauer, H. O. Ruoß, H. Irion, and W. Menzel, "Millimeter-wave-radar sensor based on a transceiver array for automotive applications," *IEEE Trans. Microw. Theory Techn.*, vol. 56, no. 2, pp. 261–269, Feb. 2008.
[52] J. Bechter, F. Roos, and C. Waldschmidt, "Compensation of motion-induced phase errors in TDM MIMO radars," *IEEE Microw. Wireless Compon. Lett.*, vol. 27, no. 12, pp. 1164–1166, Dec. 2017.
[53] T. Strohmer and B. Friedlander, "Analysis of sparse MIMO radar," *Appl. Comput. Harmon. Anal.*, vol. 37, no. 3, pp. 361–388, 2014.
[54] E. J. Candès, J. Romberg, and T. Tao, "Robust uncertainty principles: Exact signal reconstruction from highly incomplete frequency information," *IEEE Trans. Inf. Theory*, vol. 52, no. 2, pp. 489–509, Feb. 2006.
[55] H. Ermert and R. Karg, "Multifrequency acoustical holography," *IEEE Trans. Sonics Ultrason.*, vol. 26, no. 4, pp. 279–285, Jul. 1979.
[56] T. Szasz, A. Basarab, and D. Kouame, "Beamforming through regularized inverse problems in ultrasound medical imaging," *IEEE Trans. Ultrason. Ferroelectr. Freq. Control*, vol. 63, no. 12, pp. 2031–2044, Dec. 2016.
[57] M. C. Jackson, "The geometry of bistatic radar systems," *Inst. Electr. Eng. Proc. F, Commun. Radar Signal Process.*, vol. 133, no. 7, pp. 604–612, Dec. 1986.
[58] M. Herberthson, "On determining multiple positions and velocities from bistatic measurements – fast bistatic association in AASR," FOI – Swedish Defence Research Agency, FOI-R–0815–SE, pp. 1–19, 2003.
[59] A. W. Doerry, B. P. Mileshosky, and D. L. Bickel, "Tangential velocity measurement using interferometric MTI radar," SANDIA Rep., no. SAND2002-3614, pp. 1–26, 2002, doi: 10.2172/805861.

MICHAEL GOTTINGER (Member, IEEE) was born in Landshut, Germany, in 1987. He studied electrical engineering with the Munich University of Technology (TUM), Munich, Germany and with University College London (UCL), London, U.K., and received the M.Sc. degree from TUM in 2014. Since 2015, he has been working toward the Ph.D. degree with the Institute of Microwaves and Photonics (LHFT), Friedrich-Alexander University of Erlangen–Nürnberg (FAU), Erlangen, Germany. He is a reviewer for IEEE TRANSACTIONS ON MICROWAVE THEORY AND TECHNIQUES and IEEE TRANSACTIONS ON INDUSTRIAL ELECTRONICS.

MARCEL HOFFMANN (Graduate Student Member, IEEE) was born in Witten, Germany, in 1994. He received the B.Sc. and M.Sc. degrees in electrical engineering in 2016 and 2018, respectively, from the Friedrich-Alexander University of Erlangen-Nuremberg, Erlangen, Germany, where he has been working toward the Ph.D. degree with the Institute of Microwaves and Photonics (LHFT) since 2018. His research interests focus on radar signal processing and automotive radar applications, including new SAR and SLAM approaches.

MARK CHRISTMANN received the B.Eng. degree in electrical and electronic engineering from the University of East London, London, U.K., and the Dipl.-Ing. (FH) degree in communications and electronics from Fachhochschule Kaiserslautern, Kaiserslautern, Germany, in 2000. From 2000 to 2004, he was with Siemens AG, Munich, Germany, working on radar imaging and in the field project "cargo mover." In 2005, he joined Symeo GmbH, Munich. As the Head of Software Development, he advanced and implemented measurement concepts such as RTOF, TDOA, and OJTOF. He also designed a sensor fusion framework for 1-D and 2-D localization filters, noise models, and data reduction. Since 2018, he has led the Software Development for Imaging Radar and Localization team at Symeo GmbH/Analog Devices, Inc., Munich and has developed test setups and central logging and computation platforms.

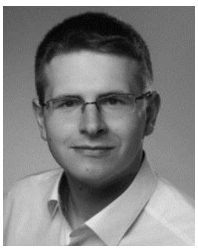

MARTIN SCHÜTZ was born in Straubing, Germany, in 1988. He received the M.Sc. degree in information and communication technology from Friedrich-Alexander University Erlangen-Nürnberg, Erlangen, Germany, in 2015. Afterward, he joined the Institute of Microwaves and Photonics (LHFT), where he worked on system design and implementation of microwave sensors for localization and remote sensing applications with autonomous ground and aerial vehicles. In 2019, he joined Symeo GmbH/Analog Devices, Inc., Munich, Germany, where he is currently working as a Systems Engineer for embedded radar sensors.

FABIAN KIRSCH was born in Bremen, Germany, in 1982. In 2003, he was accepted by the German Academic Scholarship Foundation. He received the Dipl.Inf. and Dipl.Math. degrees from the Clausthal University of Technology, Clausthal-Zellerfeld, Germany, in 2007 and 2011, respectively. In 2012, he joined the Institute of Microwaves and Photonics (LHFT), Friedrich-Alexander University Erlangen-Nürnberg, where he researched sensor fusion in local positioning systems. In 2015, he joined Elektrobit Automotive GmbH, Erlangen, Germany, where he worked on reliable vehicle positioning software for series vehicles. In 2019, he joined Analog Devices, where he works on signal processing for raw signals from multistatic radars.

PETER GULDEN (Member, IEEE) was born in Siegen, Germany, in 1972. He received the M.Sc. degree in electrical engineering from Purdue University, West Lafayette, IN, USA, in 1996, and the Dipl.-Ing. and Ph.D. degrees from the University of Siegen, Siegen, in 1998 and 2002, respectively.

In 2002, he joined the Corporate Technology Microwave Group, Siemens, Munich, Germany, as a Research Engineer and Project Manager. In 2005, he cofounded Symeo GmbH, a Siemens spinoff, which focuses on local positioning technology, where he is currently a Chief Technical Officer. He has authored or coauthored numerous papers and holds 13 patents. His current research interests include systems theory and signal processing for radio frequency systems and optical sensors.

Dr. Gulden was the recipient of a 1995–1996 Fulbright Scholarship. His scientific achievements include the 2002 EuMA Radar Prize and the 2007 EEEfCOM Innovation Prize. He is a reviewer for IEEE TRANSACTIONS ON MEASUREMENT TECHNOLOGY and IEEE SENSORS JOURNAL.

MARTIN VOSSIEK (Fellow, IEEE) received the Ph.D. degree from Ruhr-Universität Bochum, Bochum, Germany, in 1996.

In 1996, he joined Siemens Corporate Technology, Munich, Germany, where he was the Head of the Microwave Systems Group from 2000 to 2003. Since 2003, he has been a Full Professor with Clausthal University, Clausthal-Zellerfeld, Germany. Since 2011, he has been the Chair of the Institute of Microwaves and Photonics (LHFT), Friedrich-Alexander-Universität Erlangen-Nürnberg (FAU), Erlangen, Germany. He has authored or coauthored more than 250 articles. His research has led to more than 90 granted patents. His current research interests include radar, transponder, RF identification, communication, and locating systems.

Dr. Vossiek has been a member of organizing committees and technical program committees for many international conferences. He is a member of the German IEEE Microwave Theory and Techniques (MTT)/Antennas and Propagation (AP) Chapter Executive Board and the IEEE MTT-S Technical Coordinating Committees MTT-24, MTT-27, and MTT 29. He was the Founding Chair of the MTT IEEE Technical Coordinating Subcommittee MTT-27 Wireless-Enabled Automotive and Vehicular Application. He was the recipient of several international awards. Recently, he was awarded the 2019 Microwave Application Award from the IEEE MTT Society (MTT-S). He has served on the review boards for numerous technical journals. From 2013 to 2019, he was an Associate Editor for IEEE TRANSACTIONS ON MICROWAVE THEORY AND TECHNIQUES.